
Article:
Li, G. orcid.org/0000-0002-5956-4033, Ma, X.Y., Jewell, G.W. et al. (1 more author) (2018) Novel modular switched reluctance machines for performance improvement. IEEE Transactions on Energy Conversion. ISSN 0885-8969

https://doi.org/10.1109/TEC.2018.2790079

Novel Modular Switched Reluctance Machines for Performance Improvement

G. J. Li, Senior Member, IEEE, X. Y. Ma, G. W. Jewell, and Z. Q. Zhu, Fellow, IEEE
Department of Electronic & Electrical Engineering, the University of Sheffield, Sheffield, UK
g.li@sheffield.ac.uk

Abstract—Compared to non-modular machines, modular topologies become increasingly attractive due to their simplified manufacture process, better fault tolerant capability and potentially reduced material consumption. In order to maintain or even enhance the machine performance while achieving high fault tolerant capability, novel modular, single layer winding switched reluctance machines (SRMs) with different pole numbers are proposed, which are supplied by rectangular wave current with different conduction angles. The influences of the pole number and flux gap width between E-core segmented stators on the electromagnetic performance have been investigated in terms of self- and mutual inductances, electromagnetic torque, copper loss, iron loss, and radial force. It has been found that the modular structures with higher rotor pole numbers than stator slot numbers (12-slot/14-pole and 12-slot/16-pole SRMs) can maintain and even improve the average torque due to the nature of self- and mutual inductances. In addition, the torque ripple for modular machines are significantly reduced (below 50%), so do the iron loss and radial force, leading to higher efficiency albeit with potentially lower vibration and acoustic noise. Two prototypes with 12-slot/8-pole and 12-slot/14-pole combinations have been built with both non-modular and modular structures to validate the predictions in terms of inductances and static torques.

Keywords— Flux gaps, modular structure, single layer winding, switched reluctance machine.

I. INTRODUCTION

Due to virtues such as low cost, simple and robust structures, switched reluctance machines (SRMs) have gained a foothold in many industrial sectors, such as automotive, domestic appliances, renewable energy and aerospace [1] [2]. However, the doubly salient structure of SRMs can cause abrupt changes in radial force, which in turn leads to large vibration and high level of acoustic noise compared to their permanent magnet and induction counterparts [3] [4] [5].

Several strategies for vibration and acoustic noise mitigation have been proposed in literature, including advanced control techniques [4] [6] [7] [8] [9] and alternative stator and rotor designs. It was shown in [10] that with a skewed stator and rotor, the peak radial force can be reduced due to more distributed force on the stator core, which leads to lower vibration and acoustic noise. As well as radial forces, torque ripple in SRMs can also contribute to higher vibration and acoustic noise levels. To reduce torque ripple, [11] and [12] proposed modifications to the geometry of stator and rotor poles. It was shown in [13] that SRMs with high rotor pole numbers can also reduce torque ripple. By way of example, it was demonstrated that a 6-slot/10-pole SRM produces higher average torque per volume but slightly lower torque ripple than the 6-slot/4-pole SRM. Moreover, it has been found in [14] that higher average torque with lower torque ripple can be obtained by employing current waveforms with optimal conduction angles due to the nature of self- and mutual inductance waveforms.

It is worth noting that all the aforementioned SRMs employ double layer winding configuration (two coils sharing one stator slot), a winding arrangement which is also referred to as 'all stator teeth wound'. However, higher torque capability can be achieved by adopting single layer windings (only one side of a coil in each stator slot) as a consequence of the higher self-inductance [15] [16]. Additionally, the single layer winding structure can have improved fault tolerant capability since the phases are physically separated, hindering a fault such as local over-heating in one coil from propagating to the adjacent coils. Apart from the above advantages, single layer winding also provides the opportunity to adopt the modular machine topologies. These topologies can enhance further the fault tolerant capability and simplify the manufacturing of electrical machines, particularly their winding processes [17]. Moreover, if the slot and pole number combination is appropriately selected, modular machines have the ability to retain, or even improve, machine performance compared to a corresponding non-modular design [18].

Modular SRMs have also been proposed with E-core segmented stators in [19]- [20], and C-core segmented stators in [21] [22] [23]. These various segmented stators result in a reduction in core mass compared to non-modular SRMs with the same stator outer diameter, in turn leading to reduced cost and core losses. Moreover, the short flux paths which arise due to the gaps between segmented stators requires lower magneto-motive force (MMF) to generate a given torque. However, the existing modular SRMs are not designed with conventional stator/rotor pole combination, and the influence of flux gap widths on the machine performances has not been investigated in detail. Moreover, due to relative large flux gap width, stator deformation can be problematic in some modular structures.

A series of novel 3-phase modular single layer SRMs are proposed in this paper, combining the merits of single layer winding configuration (high torque capacity) and modular structure (enhanced fault tolerant capability). The cross-sections of these machines are shown in Fig. 1. In order to achieve enhanced machine performance, specifically higher average torque but with lower torque ripple, rectangular wave current with different conduction angles (unipolar 120° elec., unipolar 120° elec., and bipolar 180° elec.) are employed according to the nature of the rate of change of self- and mutual-inductances [14]. With the most appropriate conduction angles, the influence of flux gap widths and slot/pole number combinations are

investigated in terms of electromagnetic torque, copper loss, iron loss and radial force. For completeness, the iron bridges, which have the advantage of yielding a single-piece cross-section, have also been added in the flux gaps to investigate their influence on machine performance.

II. Features of Non-Modular and Modular Machines

A. Structures of Non-Modular and Modular Machines

A series of 3-phase, 12-slot SRMs with pole numbers: 8, 10, 14 and 16, are proposed with different flux gap widths (FG) in this paper although other slot/pole number combinations can also be deployed with appropriate modifications. All the machines have the same overall size and number of turns, but are optimized individually with FG=0 mm (corresponds to a non-modular structure without flux gaps as a baseline) and supplied by unipolar rectangular wave currents with conduction angle of 120° elec.

By way of example, the key design parameters for an optimized 12-slot/14-pole machine with FG=0 mm are summarized in TABLE I and the machine structure is shown in Fig. 1 (a). The investigation described in this paper is limited to single layer winding configurations.

TABLE I. MACHINE DIMENSIONS FOR FG=0mm

Stator slot number	12	Shaft outer radius (mm)	21.1
Rotor pole number	14	Active length (mm)	60
Stator outer radius (mm)	45	Turn number per phase	132
Split ratio	0.72	Rated RMS current (A)	10
Air gap length (mm)	0.5	Current density (A_{rms}/mm^2)	5.68
Rotor outer radius (mm)	31.9		

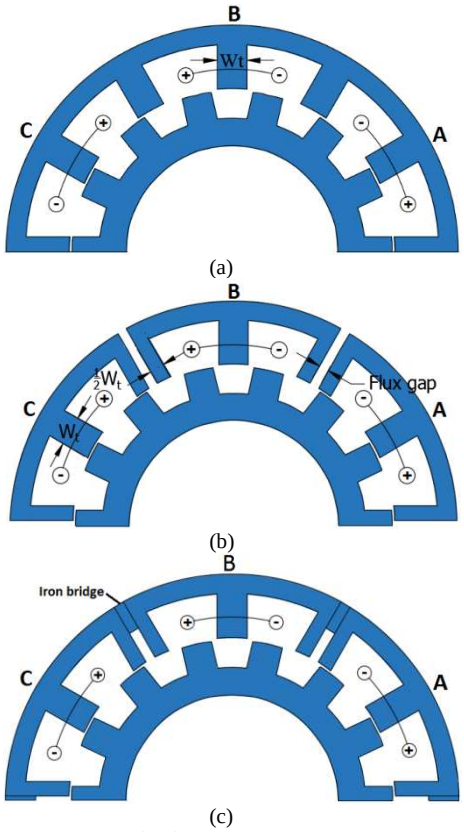

Fig. 1. Cross-sections (half) of 12-slot/14-pole SRM with (a) non-modular structures, (b) modular structures without iron bridges and (c) modular structures with iron bridges. All the machines have single layer winding topologies.

A variation on the baseline 3-phase 12-slot non-modular structure, using an E-core modular stator structure with flux-gaps is shown in Fig. 1(b). In refining this design, the tooth body iron section width W_t will be kept constant for different flux gap widths so to maintain similar level of magnetic saturation in stator teeth with flux gaps. It is inevitable that the flux path will change with increasing flux gap widths. In addition, it is worth noting that for a fixed Ampere-turn per slot, the current density will be increased with the increasing flux gap width due to the reduced slot area (increased from $5.68A_{rms}/mm^2$ to $7.33A_{rms}/mm^2$ with increasing FGs from 0mm to 6mm). For completeness, iron bridges are added in the flux gaps as shown in Fig. 1(c). In this case, the flux gaps act as dummy slots. It is apparent that the modular structures have no iron bridge. However, when the iron bridge height is equal to the stator core height – the flux gaps are fully replaced by iron, the machine stator tooth widths will be unequal, leading to an unequal tooth (UNET) structure. This structure has been used in permanent magnet machines in order to achieve higher winding factor and also higher average torque. For SRM in this paper, the influence of UNET on machine performance will also be investigated.

B. Flux Distributions

Two-dimensional finite element predicted flux distributions are shown in Fig. 2, for the particular cases of the 12-slot/8-pole and 12-slot/14-pole SRMs. Two variants of each design were considered, viz. a non-modular variant with FG=0 mm and a modular variant with FG=2 mm. For all machines, the rotors are at the aligned positions of phase A, which is supplied by a 10A dc current. It can be established that for both machines, the flux of the phase A is not linked with the phases B and C to any meaningful extent in the non-modular machine (i.e. when FG=0 mm) as shown in Fig. 2(a) and (c). However, due to the presence of flux gaps in the modular variants, the flux path is dramatically changed as shown in Fig. 2(b) and Fig. 2(d). The shorter flux path and less concentrated flux lead to lower MMF across the stator back iron. As a result, the flux density in the stator back iron of the modular machines is lower than that of the non-modular counterparts. This in turn dictates that they will be less sensitive to magnetic saturation and with improved overload torque capability.

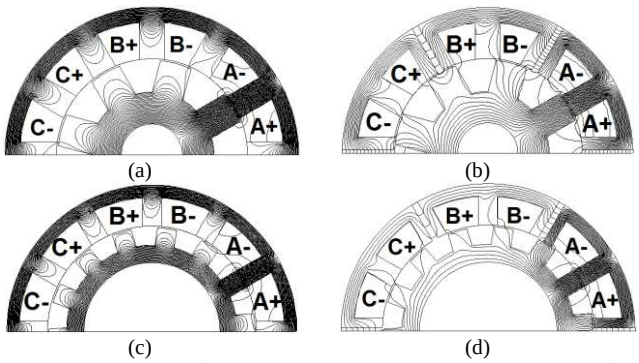

Fig. 2. Comparison of two-dimensional finite element predicted flux distributions between 12-slot/8-pole SRMs with (a) FG=0 mm and (b) FG= 2mm, and 12-slot/14-pole SRMs with (c) FG=0 mm and (d) FG= 2mm. The rotor is at the aligned position and phase A alone is supplied with a 10A dc current.

C. Self- and Mutual Inductances

Due to the relationship between flux linkage and apparent inductances, the varying flux paths will have influence on self-inductance L and mutual inductance M. The derivatives of inductances with respect to rotor positions for the 12-slot/8-pole and 12-slot/14-pole machines have been calculated using two-dimensional finite element analysis, as shown in Fig. 3 and Fig. 4, where 0 elec. deg. represents the rotor aligned position. In $dL/d\theta$ and $dM/d\theta$, the units for L and M are mH and for θ is in elec. deg. The flux gap widths increase from 0mm to 6mm and only the phase A is supplied with dc currents of both 10A and 40A. The trend in inductance derivatives for different flux gap widths of the 12-slot/10-pole and 12-slot/16-pole machines, although not shown in this paper, are very similar to those of the 12-slot/8-pole and 12-slot/14-pole machines, respectively.

In Fig. 3 and Fig. 4, the amplitudes of $dL_a/d\theta$ for both the 12-slot/8-pole and 12-slot/14-pole SRMs decrease with increasing flux gaps widths at low current (<15A). However, at high currents, the amplitude of $dL_a/d\theta$ for the 12-slot/8-pole is only marginally influenced by the width of the flux gap. In the case of the 12-slot/14-pole SRM, the modular machines have higher amplitudes of $dL_a/d\theta$ compared to the non-modular machine.

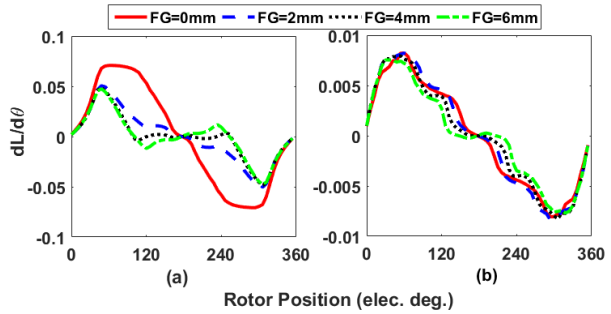

Fig. 3. Comparison of $dL_a/d\theta$ between the 12-slot/8-pole modular SRM with different FG widths. Phase A is supplied with a (a) 10A and (b) 40A dc current.

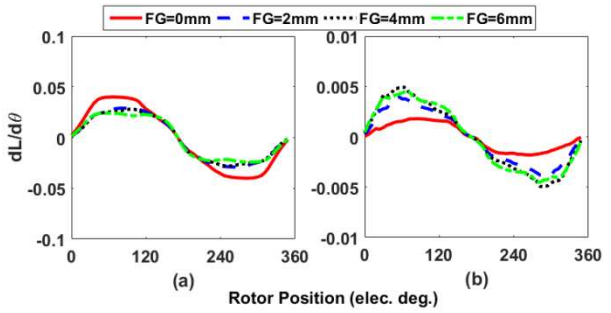

Fig. 4 Comparison of $dL_a/d\theta$ between the 12-slot/14-pole modular SRM with different FG widths. Phase A is supplied with a (a) 10A and (b) 40A dc current.

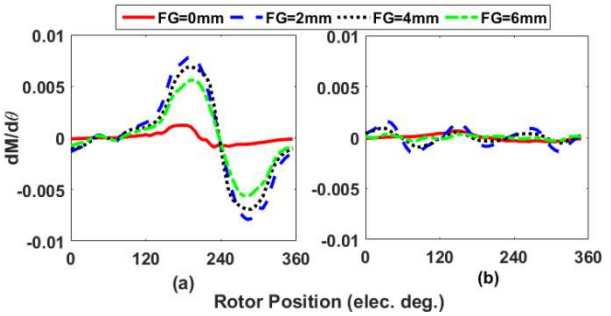

Fig. 5. Comparison of $dM_{ab}/d\theta$ between (a) 12-slot/8-pole and (b) 12-slot/14-pole SRMs with different FG widths. Phase A is supplied with a 10A dc current.

The variation of $dM_{ab}/d\theta$ at 10A dc current is shown in Fig. 5. This single value of current is sufficient to demonstrate this aspect of behavior since this measure is not influenced to any meaningful degree by the current levels that are likely to be encountered in this machine. Moreover, it is worth noting that compared to $dL_a/d\theta$, the very modest contribution from $dM_{ab}/d\theta$ is usually neglected for non-modular SRMs. According to the waveforms of $dL_a/d\theta$, it can be predicted that the 12-slot/14-pole SRMs will have the potential to produce higher electromagnetic torque with flux gaps than a corresponding non-modular design.

III. Electromagnetic Performance Investigation of Non-modular and Modular Machines

A. On-Load Torque for Different Conduction Angles

The general expression of electromagnetic torque of a SRM is given by:

$$T = \frac{1}{2}{i_a}^2\frac{dL_a}{d\theta} + \frac{1}{2}{i_b}^2\frac{dL_b}{d\theta} + \frac{1}{2}{i_c}^2\frac{dL_c}{d\theta} + i_a i_b\frac{dM_{ab}}{d\theta} + i_b i_c\frac{dM_{bc}}{d\theta} + i_a i_c\frac{dM_{ac}}{d\theta} \quad (1)$$

where i_a, i_b and i_c are the 3-phase currents. L_a, L_b and L_c are 3-phase self-inductances. M_{ab}, M_{bc} and M_{ac} are the mutual inductances between phases.

The definition of torque ripple deployed in this paper is calculated on the basis of the maximum (T_{max}), the minimum (T_{min}) and the average torque (T_{av}) over an electrical period:

$$T_{ripple} = \frac{T_{max} - T_{min}}{T_{av}} \times 100\% \quad (2)$$

Given the nature of the waveforms of self- and mutual inductance derivatives, the conduction angles of rectangular wave current supply have been optimized and selected according to the method stated in [14], as shown in TABLE II. For unipolar excitation, the current has the positive magnitude and is always in the same direction. However, the current has both positive and negative pulses for bipolar excitation, e.g. the current waveform with conduction angle of bipolar 180° elec. consists of a negative current pulse for 60° elec. and a positive current pulse for 120° elec. Moreover, both the current pulses are supplied when $dL_a/d\theta \geq 0$ in order to generate positive torque. With conduction angle of unipolar 120° elec., the mutual inductances do not make a net contribution to electromagnetic torque. Hence, the torque is only produced by the change in self-inductance. However, both unipolar and bipolar 180° elec. conduction make full use of both the changes in self- and mutual-inductances for torque generation.

TABLE II. CONDUCTION ANGLES FOR RECTANGULAR WAVE CURRENT SUPPLY

Conduction angle (elec.)	Component (elec.)
Unipolar 120°	Positive 120°
Unipolar 180°	Positive 180°
Bipolar 180°	Negative 60° + positive 120°

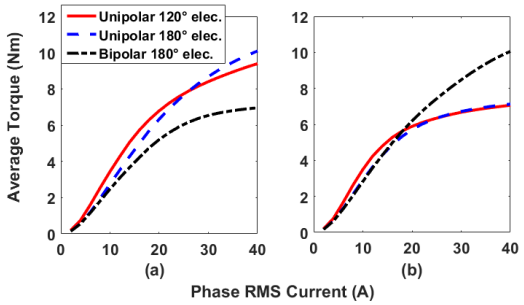

Fig. 6. Influence of conduction angles on average torque between (a) 12-slot/8-pole and (b) 12-slot/14-pole non-modular SRMs.

In order to select the most appropriate conduction angles for different machines, two-dimensional finite element calculations were performed to establish the average torque over one cycle for each machine as function of the magnitude of current. Fig. 6 shows the resulting comparison of average torques between non-modular SRMs. It is evident that with conduction angle of unipolar 120° elec., the non-modular 12-slot/8-pole and 12-slot/14-pole SRMs have greater average torque performances at low current. However, at high current, the highest average torque of the 12-slot/8-pole non-modular SRM is achieved by adopting the conduction angle of unipolar 180° elec., while for the 12-slot/14-pole machine it is the bipolar 180° elec. Additionally, as shown in TABLE III, the lowest torque ripples for both the 12-slot/8-pole and 12-slot/14-pole machines are achieved by adopting the conduction angle of unipolar 180° elec., while the highest torque ripple are generated when adopting the conduction angle of bipolar 180° elec.

TABLE III. TORQUE RIPPLE OF NON-MODULAR SRMS AT $40A_{rms}$

Machine type	Conduction angle (elec. deg.)		
	Unipolar 120	Unipolar 180	Bipolar 180
12/8	81.59%	35.77%	123.2%
12/14	51.24%	37.49%	67.96%

TABLE IV. SELECTION OF APPROPRIATE CONDUCTION METHODS

Machine type	Low current	High current
12/8	unipolar 120° elec.	unipolar 180° elec.
12/10	unipolar 120° elec.	bipolar 180° elec.
12/14	unipolar 120° elec.	bipolar 180° elec.
12/16	unipolar 120° elec.	unipolar 180° elec.

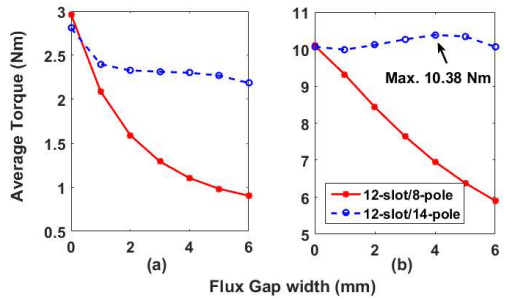

Fig. 7. Comparison of average torque between the 12-slot/8-pole and 12-slot/14-pole SRMs against FG widths at (a) $10A_{rms}$ and (b) $40A_{rms}$.

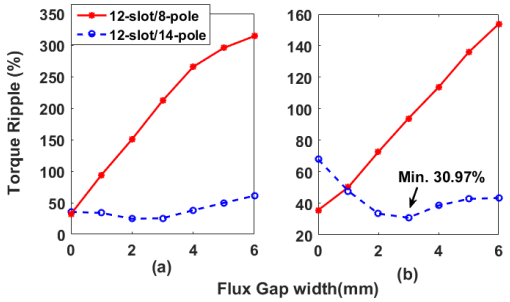

Fig. 8. Comparison of torque ripple between 12-slot/8-pole and 12-slot/14-pole SRMs against FG widths at (a) $10A_{rms}$ and (b) $40A_{rms}$.

Furthermore, as shown in TABLE IV, the unipolar 120° elec. is the most effective conduction angles for all the SRMs with different slot/pole combinations at low current. However, at high current, unipolar 180° elec. conduction is preferred for 12/8 and 12/16 SRMs, and bipolar 180° elec. conduction is preferred for 12/10 and 12/14 SRMs. For consistency, the preferred conduction angles for high current are adopted for the following on-load torque investigations for the modular machines with different flux gap widths.

The average torque and torque ripple at different current levels were predicted by two-dimensional finite element analysis. The resulting outcomes are shown in Fig. 7 and Fig. 8, from which it is evident that the 12-slot/8-pole SRM with non-modular structure achieves better performance than its modular counterpart regardless of phase RMS current employed. However, for a full range of currents, the 12-slot/14-pole SRM with FG=3 mm has the best torque performances considering both the average torque and torque ripple. Hence, in order to investigate the sensitivity to magnetic saturation and overload torque capability, the modular machine with FG=3 mm was selected as the in-depth design for copper loss calculation.

B. Copper Loss

The machines are optimized with non-modular structure for a fixed current density of 5.68A/mm^2. Hence, with increasing flux gaps, the slot area is slightly reduced, leading to reduced wire diameter. Fig. 9 shows the copper loss for different SRMs for a phase current of $10A_{rms}$. It is evident that the copper losses at rated current for all modular machines are higher than those of their non-modular counterparts irrespective of the number of poles. However, previous results in section II demonstrated that the average torque is also influenced by the dimensions of the flux gaps. Hence, in order to provide a consistent basis for comparing design, the relationship between torque and copper loss needs to be investigated.

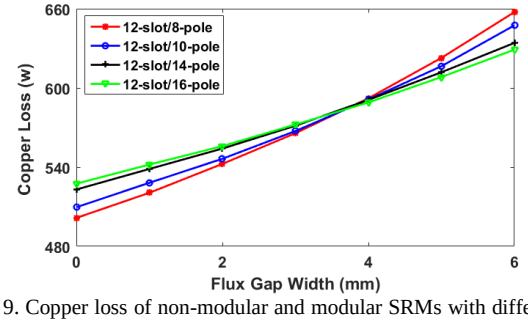

Fig. 9. Copper loss of non-modular and modular SRMs with different pole numbers and FG widths at $10A_{rms}$ current.

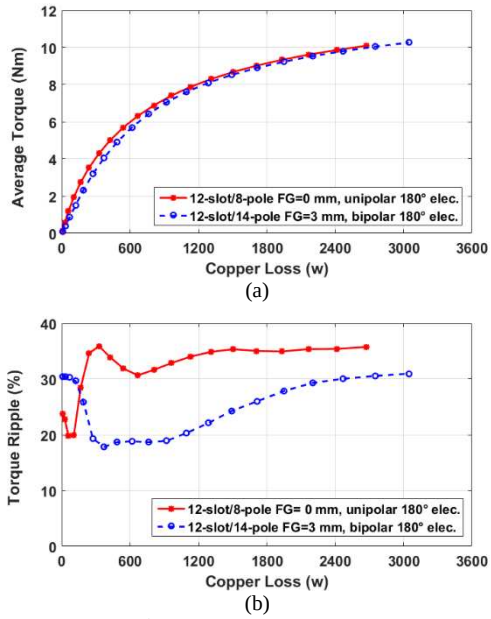

Fig. 10. Comparison of (a) average torque and (b) torque ripple as a function of SRM copper loss.

With the optimized conduction angles, the variation in the average torques as a function of copper loss for a non-modular 8-pole SRM and a modular 14-pole SRM (FG=3mm) are shown in Fig. 10. It is evident that both machines can produce similar average torque values for the same copper loss. However, the torque ripple in modular 12-slot/14-pole can be much lower than that in 12-slot/8-pole at the same copper loss (phase current).

C. Iron Loss

Based on the method detailed in [14], equation (3) is used for calculating the iron loss density in each element of the FE element model [1]. The overall loss is obtained from a summation of the losses in each finite element in the stator and rotor core regions.

$$p_{iron}(W/m^3) = \sum_{n=1,2,3\ldots} (nf)\left(k_{h1}\Delta B_{pp,n} + k_{h2}\Delta B_{pp,n}^2\right) + k_e \sum_{n=1,2,3\ldots} (nf_x)\int_0^{\frac{1}{nf_x}} \left(\frac{\partial B_n}{\partial t}\right)^2 dt \quad (3)$$

where n is the harmonic order, f is the stator or rotor iron core flux density frequency, B_{pp} is peak to peak value of the flux density. For silicon iron core considered in this paper, the hysteresis loss coefficients k_{h1} and k_{h2} are $5A/m$ and $40Am/Vs$ respectively. The eddy current loss coefficient k_e is $0.022\ Am/V$.

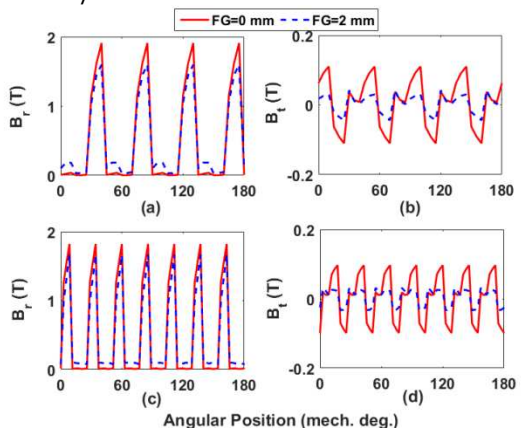

Fig. 11. Radial and tangential flux densities in stator tooth of (a) and (b) 12-slot/8-pole, (c) and (d) 12-slot/14-pole SRM. 3-phases are supplied with square wave currents with conduction angle of unipolar 120° elec.

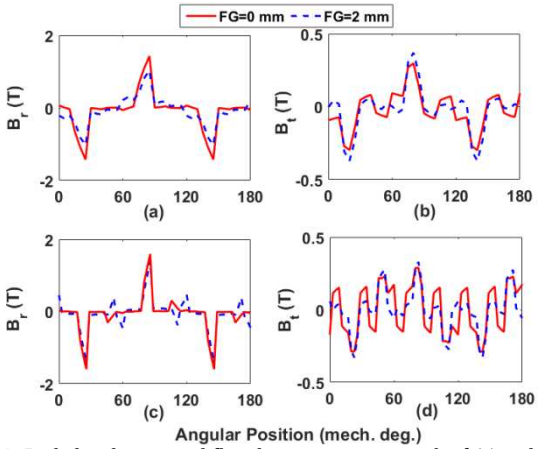

Fig. 12. Radial and tangential flux densities in rotor tooth of (a) and (b) 12-slot/8-pole, (c) and (d) 12-slot/14-pole SRM. 3-phases are supplied with rectangular wave currents with conduction angle of unipolar 120° elec.

The flux densities have been investigated in different parts of the stator and rotor iron cores. By way of example, the flux densities at the middle of the stator and rotor teeth for different machines with different flux gap widths as shown in Fig. 11 and Fig. 12. It is apparent from these waveforms that the modular machines have lower flux densities in both the stator and rotor teeth than their non-modular counterparts. In addition, with different pole numbers, the stator flux densities have different periodicities. However, the rotor flux densities exhibit 3 full cycles in one mechanical cycle (360 mech. deg.) for both machines. The resulting flux density frequencies at 400rpm are given in TABLE V.

TABLE V. SUMMARY OF FLUX DENSITY FREQUENCIES AT A ROTAIONAL SPEED OF 400RPM

Machine types	B_r/B_t frequency (Hz)	
	Stator	Rotor
12-slot/8-pole	53.3	20
12-slot/14-pole	93.3	20

TABLE VI. IRON LOSS (W) @ $10A_{rms}$ AND 400RPM

Machine types	FG (mm)			
	0	2	4	6
12-slot/8-pole	3.54	1.48	1.18	1.26
12-slot/14-pole	6.61	2.47	1.84	1.49

Fig. 13 and Fig. 14 show the variation of iron loss as functions of phase RMS current and speed for different flux gap widths. Due to the higher stator flux density frequency, the 12-slot/14-pole machine produces higher iron loss than the 12-slot/8-pole machine, as expected. However, with the increasing flux gap width, both machines produce significantly lower iron losses. For example, when FG=2mm, the iron loss of 12-slot/14-pole is reduced by around 63% when compared to the machines with FG=0mm. This is a very attractive feature, particularly for SRM used in high speed applications, where iron loss could constitute a significant proportion of the overall loss.

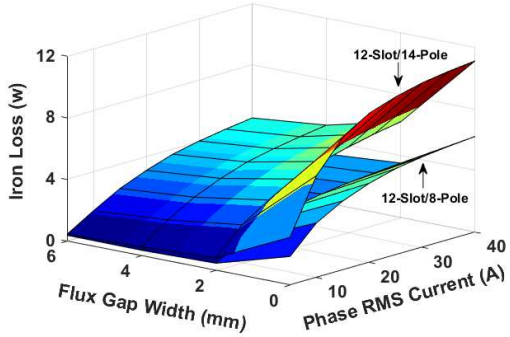

Fig. 13. Variation of iron loss against flux gap width and phase RMS current between the 12-slot/8-pole and 12-slot/14-pole SRMs. The 3-phases are supplied by rectangular wave current with conduction angle of unipolar 120° elec., at a rotational speed of 400rpm.

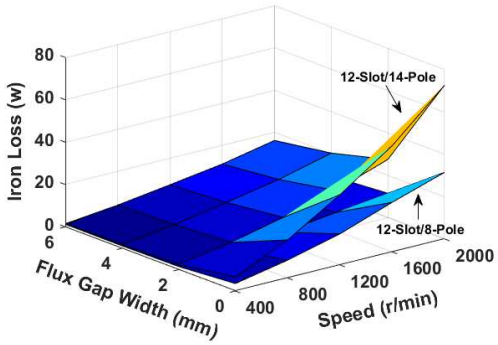

Fig. 14. Variation of iron loss against FG width and speed between the 12-slot/8-pole and 12-slot/14-pole SRM. 3-phases are supplied by rectangular wave current with conduction angle of unipolar 120° elec., @ $10A_{rms}$.

D. Radial Force

The change of flux path due to the presence of flux gaps will not only influence the iron loss but also the radial force. Since the abrupt change of radial force acting on the stator as the rotor passes successive teeth is the main electromagnetic source of vibration and acoustic noise, an understanding of radial force is the key to investigating machine mechanical performance. According to Maxwell stress tensor, the radial force F_r on one stator pole is given by [24]:

$$F_r = \int_{-\frac{\alpha}{2}}^{\frac{\alpha}{2}} \frac{1}{2\mu_0} ({B_r}^2 - {B_t}^2) r L d\theta \qquad (4)$$

where α is the stator pole pitch, i.e. 30 mech. deg. for a SRM with 12-slot, μ_0 is the free space permeability, B_r and B_t are the radial and tangential flux densities in the airgap, r is the stator inner radius, and L is the stack length.

According to (4), $({B_r}^2 - {B_t}^2)$ distribution in the air gap has been investigated, in which only the phase A is supplied by a dc current and the rotor is at the aligned position of the phase A. The influence of flux gap width on the flux densities at different current levels is shown in Fig. 15. Since the magnitude of the radial force is directly proportional to $({B_r}^2 - {B_t}^2)$, it can be observed that both the 12-slot/8-pole and 12-slot/14-pole modular SRMs are likely to have lower radial force distribution around the airgap. However, due to magnetic saturation, the non-modular and modular 12-slot/14-pole machines will produce similar peak radial force at high current.

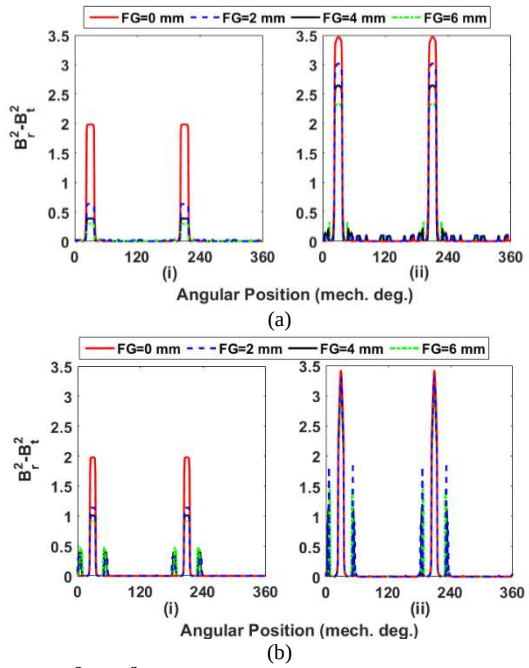

Fig. 15. $({B_r}^2 - {B_t}^2)$ distribution in the airgap of the (a) 12-slot/8-pole and (b) 12-slot/14-pole non-modular and modular SRMs. Phase A is supplied by (i) 10A and (ii) 40A dc current and the rotor pole is aligned with phase A.

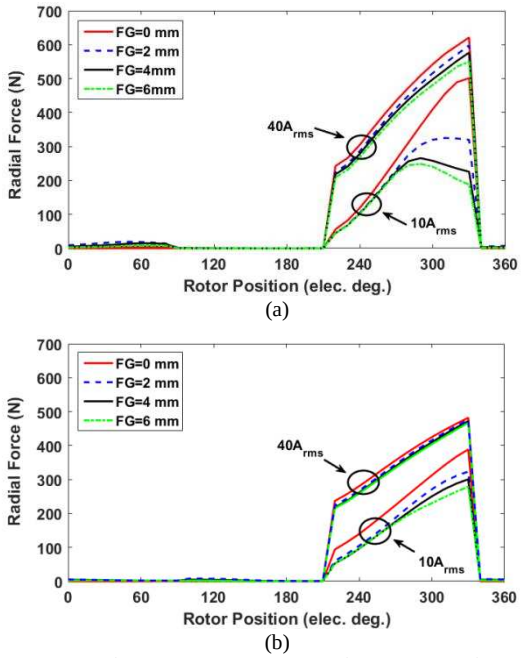

Fig. 16. Radial force on one stator pole of the phase A for different FG widths and currents of (a) 12/8 and (b) 12/14 SRM. 3-phase rectangular wave current is supplied with conduction angle of unipolar 120° elec.

In order to investigate the influence of flux gap width on the radial force, Fig. 16 shows the localized radial force on one stator pole of the phase A predicted by two-dimensional finite element analysis. In this case, the 3-phases are supplied by currents with unipolar 120° elec. conduction. The 0° elec. rotor position corresponds to the rotor being aligned with phase A. It can be seen that the radial force for both machines is decreased with increasing flux gaps widths at low current, e.g. $10A_{rms}$. For 12-slot/8-pole machines, the peak radial force is reduced by 35.2% when FG is changed from 0 mm to 2 mm. For 12-slot/14-pole machines, it is reduced by 16.8%. However, the difference between peak radial force of different flux gaps widths narrows at

high current, e.g. $40A_{rms}$, again due to the onset of appreciable magnetic saturation. Moreover, at the same current level, the peak radial force of 12-slot/8-pole SRM is higher than that of 12-slot/14-pole SRM. This is a consequence of the optimized stator pole arc being shorter with increasing rotor pole number, hence the radial force surface area is reduced.

TABLE VII shows the influence of conduction angles on peak radial force at different current levels for modular SRM with FG=2mm. This demonstrates that at low current, the lowest peak radial force is produced with a bipolar 180° elec. conduction angle. However, due to the different magnetic saturation levels, machines with different pole numbers have different preferred current conduction angles at high current.

TABLE VII. INFLUENCE OF CONDUCTION ANGLES ON PEAK RADIAL FORCE FOR FG=2MM

	Conduction angle (elec. deg.)	Peak radial force at different current level (N)	
		$10A_{rms}$	$40A_{rms}$
12/8	Unipolar120	325	597.7
	Unipolar180	257.6	625.1
	Bipolar180	235.3	591.7
12/14	Unipolar120	323.5	475.8
	Unipolar180	297.1	517.6
	Bipolar180	264.1	499.3

IV. Modular Machine with Iron Bridges

For completeness, iron bridges were added into the flux gaps to yield single-piece stator laminations. The resulting geometries become those are shown previously in Fig. 1(c). With different iron bridge heights and flux gap widths, the average torque of the 12-slot/8-pole and 12-slot/14-pole SRMs varies as shown in Fig. 17.

The iron bridge height does not have significant influence on average torque especially for the height > 4mm. At low current, both machines have higher average torque with increasing iron bridge height ($\leq 4mm$), but the average torque is decreased with increasing flux gap width. However, at high current, the 12-slot/14-pole SRM produces lower average torque with increasing iron bridge height ($\leq 4mm$). Hence, it can be concluded that the iron bridge has positive influence on average torque for both machines at low current, but negative influence for 12-slot/14-pole machine at high current.

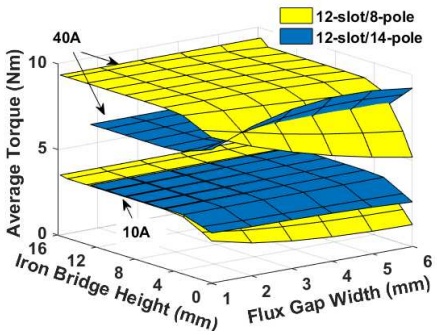

Fig. 17. Comparison of average torques between the 12/8 and 12/14 SRMs with iron bridges.

As aforementioned, when the flux gaps are fully replaced by iron the stator tooth widths become unequal, leading to unequal tooth (UNET) machines. Hence, the coils in the UNET machines can be wound around either the narrower or the wider stator teeth as shown in Fig. 18 and the torque performance has been compared to modular machines as shown in Fig. 19. It is found that for 12-slot/8-pole, the UNET with coils on wider stator teeth can produce the highest torque with FG=1mm (virtual flux gaps in the UNET machines). However, for 12-slot/14-pole, the better torque performance (higher average torque but lower torque ripple) is achieved with a modular structure.

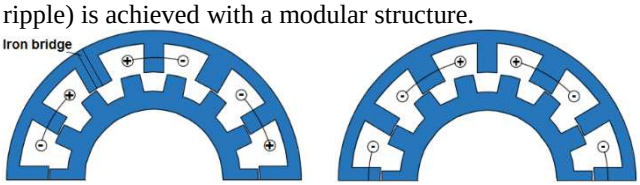

Fig. 18. Cross-sections of 12/8 SRM with UNET with (a) winding on narrower teeth (original teeth) (b) winding on wider teeth. The iron bridge (or FG) width is 2mm.

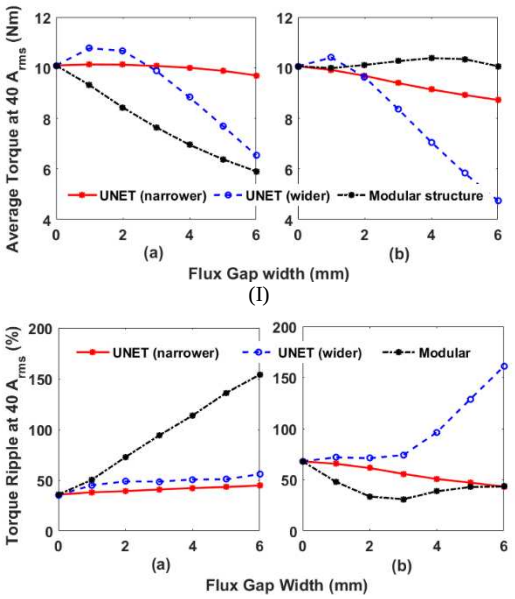

Fig. 19. (I) Average torque and (II) torque ripple comparison between modular and UNET SRMs with (a) 12-slot/8-pole and (b) 12-slot/14-pole. Appropriate conduction angles are employed.

V. Experimental Validation

A. Prototypes of Non-modular and Modular SRMs

Prototypes of 12-slot/8-pole and 12-slot/14-pole non-modular and modular SRMs have been built to validate the predictions. Fig. 20 (a) and (b) show the 12-slot stators with FG=0mm (no flux gaps) and 2mm. Fig. 20 (c) and (d) are the 8-pole and 14-pole rotors.

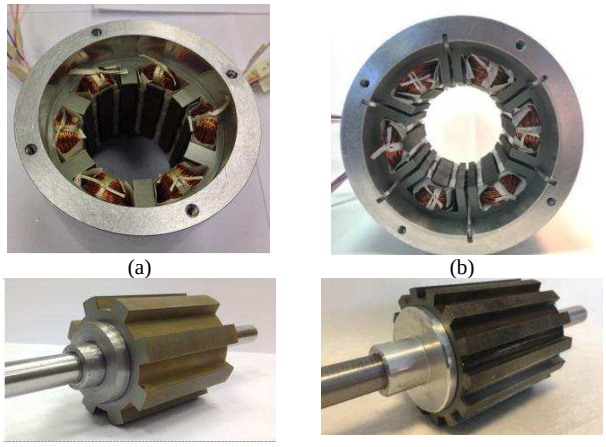

Fig. 20. Prototypes of non-modular and modular SRMs. (a) and (b) are 12-slot stators with FG=0mm and 2mm, (c) and (d) are 8-pole and 14-pole rotors.

B. Measurement of Self- and Mutual-Inductances

The self-inductance L_a and mutual-inductance M_{ab} were measured according to the method in [14]. The predicted and measured self- and mutual-inductances of both 12-slot/8-pole and 12-slot/14-pole non-modular and modular SRMs are presented in Fig. 21 at 1A AC current. The measured results are generally higher than the predicted ones mainly due to the fact that the end-windings have not been taken into account in the predictions.

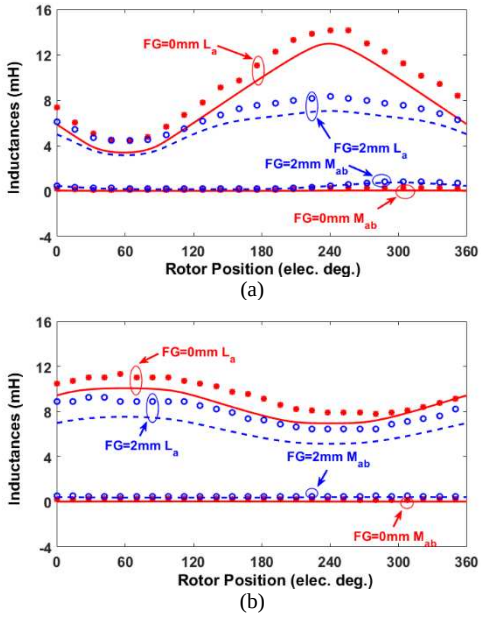

Fig. 21. Predicted and measured self- and mutual-inductances against rotor position at 1A AC current. (a) 12-slot/8-pole SRM with FG=0mm and 2mm. (b) 12-slot/14-pole SRM with FG=0mm and 2mm (lines: predicted results, and marks: measured results).

C. Self- and Mutual- Torques

In order to measure the static torque that produced by both the self- and mutual-inductances (self- and mutual-torques), the method of static torque measurement in [25] has been adopted in this paper.

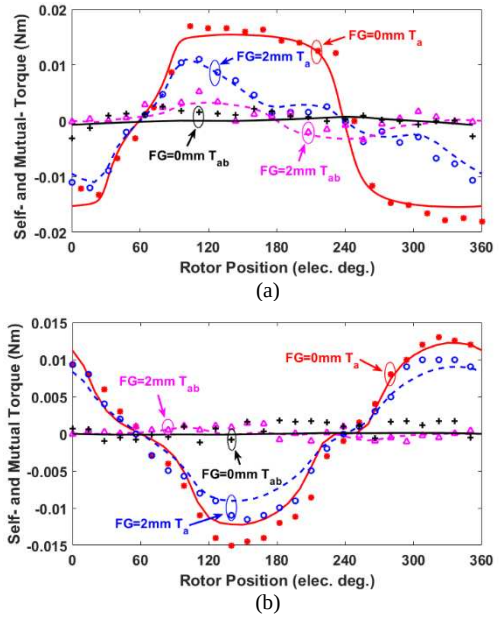

Fig. 22. Predicted and measured self- and mutual-torques against rotor position at 1A dc current. (a) 12-slot/8-pole SRM with FG=0mm and 2mm. (b) 12-slot/14-pole SRM with FG=0mm and 2mm (lines: predicted results, and marks: measured results).

By way of example, predicted and measured self-torques of phase A, T_a, and mutual-torques between phases A and B, T_{ab}, are shown in Fig. 22. It is worth noting that the mutual torque T_{ab} is obtained by the torque produced by the phases A and B connected in series minus the sum of self-torques of the phases A and B. In order to minimize the influence of magnetic saturation and also to prevent the machine from overheating, 1A dc current is used for phase current supply during these tests.

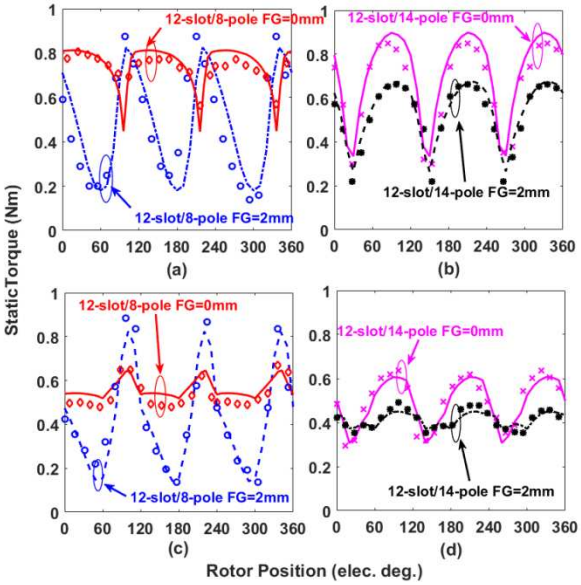

Fig. 23. Predicted and measured static on-load torques at 5A phase rms current with different conduction angles (a) and (b) unipolar 120° elec. deg. (c) and (d) unipolar and bipolar 180° elec. deg. for 12-slot/8-pole and 12-slot/14-pole SRMs, respectively (lines: predicted results, and marks: measured results).

D. Static On-load Torque

Adopting to the preferred conduction angles in TABLE IV, the static on-load torques of 12-slot/8-pole and 12-slot/14-pole SRMs have also been measured at different rotor positions, as shown in Fig. 23. The phase rms current was 5A for all the currents with different conduction angles. The aligned rotor position of phase A can be tested by injecting current only into the phase A. This will cause the rotor to rotate to the aligned position of the phase A. In addition, the dc current can be injected into each phase at different rotor positions according to the current waveforms in order to obtain the torque waveforms shown in Fig. 23. Moreover, the values of average torque and torque ripple for both predicted and measured results are summarized in TABLE VIII.

TABLE VIII. COMPARISON OF MACHINE AVERAGE TORQUE AND TORQUE RIPPLE AT 5A_{rms}

	FG (mm)	Average torque (Nm)		Torque ripple (%)	
		Predicted	Measured	Predicted	Measured
Unipolar 120 elec. deg.					
12/8	0	0.75	0.73	48.95	33.28
	2	0.49	0.48	131.91	152.92
12/14	0	0.71	0.66	78.91	83.85
	2	0.54	0.52	75.40	84.85
Unipolar 180/bipolar 180 elec. deg.					
12/8	0	0.56	0.54	22.75	35.47
	2	0.42	0.43	162.46	172.26
12/14	0	0.49	0.50	61.24	68.82
	2	0.41	0.41	19.22	33.24

VI. Conclusion

In this paper, 3-phase modular and non-modular single layer SRMs with different pole numbers (12-slot/8-pole, 12-slot/10-pole, 12-slot/14-pole, and 12-slot/16-pole) have been investigated. The optimal conduction angles have been established on the basis of non-modular machines for electromagnetic torque investigation with different flux gap widths. It has been demonstrated that for this specific size of machine, the highest average torque can be achieved by the non-modular 12-slot/8-pole SRM and the modular 12-slot/14-pole SRM. Moreover, the modular 12-slot/14-pole SRM produces even higher average torque than 12-slot/8-pole SRM at $40A_{rms}$ due to being less sensitive to magnetic saturation in the back iron. However, the lower torque ripple is obtained by the modular 12-slot/14-pole SRM. In addition, regardless of pole numbers, the modular machines will tend to exhibit lower iron loss and radial force. Therefore, modular SRMs have the potential of achieving lower levels of vibration and acoustic noise than non-modular SRMs. The prototypes of 12-slot/8-pole and 12-slot/14-pole, with both non-modular and modular structures have been constructed and the predicted inductances and torques have been validated by experimental measurements.

VII. References

[1] G. J. Li, J. Ojeda, E. Hoang, M. Lecrivain and M. Gabsi, “Comparative studies between classical and mutually coupled switched reluctance motors using thermal-electromagnetic analysis for driving cycles,” IEEE Trans. Magn., vol. 47, no. 4, pp. 839-847, Apr. 2011.

[2] T. J. E. Miller, “Optimal design of switched reluctance motors,” IEEE Trans. Ind. Electron., vol. 49, no. 1, pp. 15-27, Feb. 2002.

[3] D.E.Cameron; J. H. Lang; S. D. Umans;, “The origin and reduction of acoustic noise in doubly salient variable-reluctance motors,” IEEE Trans. Ind. Applicat., vol. 28, pp. 1250-1255, Nov./Dec. 1992..

[4] C. Y. Wu and C. Pollock, “Analysis and reduction of vibration and acoustic noise in the switched reluctance drive,” IEEE Trans. Ind. Appl., vol. 31, no. 1, pp. 91-98, Jan./Feb. 1995.

[5] X. B. Liang, G. J. Li, J. Ojeda, M. Gabsi and Z. X. Ren, “Comparative study of classical and mutually coupled switched reluctance motors using multiphysics finite-element modeling,” IEEE Trans. Ind. Electron., vol. 61, no. 9, pp. 5066-5074, Sep. 2014.

[6] J. W. Ahn, S. J. Park and D. H. Lee, “Hybrid excitation of SRM for reduction of vibration and acoustic noise,” IEEE Trans. Ind. Electron., vol. 51, no. 2, pp. 374-380, Apr. 2004.

[7] X. Mininger, N. Galopin, X. Ojeda, F. Bouillault and M. Gabsi, “Modeling of magnetoelastic and piezoelectric coupling: Application to SRM noise damping,” IEEE Trans. Magn., vol. 45, no. 3, pp. 1218-1221, Mar. 2009.

[8] D. H. Cameron, J. H. Lang and S. D. Umans, “The origin and reduction of acoustic noise in doubly salient variable-reluctance motors,” IEEE Trans. Ind. Appl., vol. 26, no. 6, pp. 1250-1255, Dec. 1992.

[9] X. Ojeda, X. Mininger, H. B. Ahmed, M. Gabsi and M. Lecrivain, “Piezoelectric actuator design and placement for switched reluctance motors active dampling,” IEEE Trans. Energy Convers., vol. 24, no. 2, pp. 305-313, Jun. 2009.

[10] C. Wei, P. Pillay, Z. J. Tang and A. M. Omekanda , “Low-vibration design of switched reluctance motors for automotive applications using modal analysis,” IEEE Trans. Ind. Appl., vol. 39, no. 4, pp. 971-977, Jul./ Aug. 2003.

[11] F. Sahin, H. B. Ertan and K. Leblebicioglu, “Optimum geometry for torque ripple minimization of switched reluctance motors,” IEEE Trans. Energy Conver., vol. 15, no. 1, pp. 30-39, Mar. 2000.

[12] G. J. Li, J. Ojeda, S. Hlioui, E. Hoang, M. Lecrivain and M. Gabsi, “Modification in rotor pole geometry of mutually coupled switched reluctance machine for torque ripple mitigating,” IEEE Trans. Magn., vol. 48, no. 6, pp. 2025-2034, Dec. 9, 2011.

[13] P. C. Desai, M. Krishnamurthy, N. Schofield and A. Emadi, “Novel switched reluctance machine configuration with higher number of rotor pole than stator poles: concept to implementation,” IEEE Trans. Ind. Elec., vol. 57, no. 2, pp. 649-659, Oct. 20, 2009.

[14] G. J. Li, X. Y. Ma, G. W. Jewell and Z. Q. Zhu, “Influence of conduction angles on single layer switched reluctance machines,” IEEE Trans. Magn., vol. 52, no. 12, pp. 1-11, Jul. 2016.

[15] X. Y. Ma, G. J. Li, G. Jewell and Z. Q. Zhu, “Comparative study of short-pitched and fully-pitched SRMs supplied by sine wave currents,” in ICIT15, Sevilla, Spain, Mar. 17-19, 2015.

[16] X. Y. Ma, G. J. Li, G. W. Jewell, Z. Q. Zhu and H. L. Zhan, “Performance comparison of doubly salient reluctance machine topologies supplied by sinewave currents,” IEEE Trans. Ind. Electron., vol. 63, no. 7, pp. 4086-4096, Mar. 2016.

[17] E. Spooner, A. C. Williamson and G. Catto, “Modular design of permannet-magnet generators for wind turbines,” IEE Proc. Electr. Power Appl., vol. 143, no. 5, pp. 388-395, Sep. 1996.

[18] G. J. Li, Z. Q. Zhu, W. Q. Chu, M. P. Foster and D. A. .Stone, “Influence of flux gaps on electromagnetic performance of novel modular PM machines,” IEEE Trans. Energy Convers., vol. 29, no. 3, pp. 716-726, Sep. 2014.

[19] H. Eskandari and M. Mirsalim, “An improved 9/12 two phase E-core switched reluctance machine,” IEEE Trans. Energy Conver. , vol. 28, no. 4, pp. 951-958, Dec. 2013.

[20] C. Lee and R. Krishnan, “New design of a two-phase E-core switched reluctance machine by optimizing the magnetic structure for a specific application: concept, design, and analysis,” IEEE Trans. Ind. Appl., vol. 45, no. 5, pp. 1804-1814, Sep./Oct. 2009.

[21] M. Tanujaya, D. H. Lee and J. W. Ahn, “Characteristic analysis of a novel 6/5 C-core type three-phase switched reluctance motor,” in ICEMS, Beijing, 2011.

[22] S. H. Mao and M. C. Tsai, “A novel switched reluctance motor with C-core stators,” IEEE Trans. Magn., vol. 41, no. 12, pp. 4413-4420, Dec. 2005.

[23] S. P. Nikam and B. G. Fernandes, “Design of soft magnetic composite based modular four phase SRM for electirc vehicle application,” in ICEM, Berlin, Sep. 2014.

[24] N. R. Garrigan, W. L. Soong, C. M. Stephens, A. Storace and T. A. Lipo, “Radial force characteristics of a switched reluctance machine,” in Indus. Appl. Conference, Thirty-Fourth IAS Annual Meeting, 3-7 Oct. 1999.

[25] Z. Q. Zhu, “A simple method for measuring cogging torque in permanent magnet machines,” in IEEE Power & Energy Society General Meeting,, Jul. 26-30, 2009.